Research Article | Vol. 33, No. 20 / 6 Oct 2025 / Optics Express 42358
Optics EXPRESS

Suppression of Doppler-induced crosstalk in linear-frequency-swept Φ-OTDR using scattering-enhanced fiber

YIHANG WANG,[1,2] BAIJIE XU,[1,2] GUANFENG CHEN,[1,2] ZICHEN LI,[1,2] BIN DU,[1,2] XIZHEN XU,[1,2] YIPING WANG,[1,2] AND JUN HE[1,2,*]

[1]*State Key Laboratory of Radio Frequency Heterogeneous Integration, Key Laboratory of Optoelectronic Devices and Systems of Ministry of Education/Guangdong Province, College of Physics and Optoelectronic Engineering, Shenzhen University, Shenzhen 518060, China*
[2]*Shenzhen Key Laboratory of Photonic Devices and Sensing Systems for Internet of Things, Guangdong and Hong Kong Joint Research Centre for Optical Fibre Sensors, Shenzhen University, Shenzhen 518060, China*
[*]*hejun07@szu.edu.cn*

Abstract: Linear-frequency-swept (LFS) phase-sensitive optical time domain reflectometry (Φ-OTDR) can overcome the constraints between spatial resolution and signal-to-noise ratio. However, the Doppler shift induced by vibration in the Rayleigh backscattering (RBS) signal generates significant crosstalk beyond the vibration area. Here, we propose and demonstrate a Doppler-crosstalk-suppressed quasi-distributed acoustic sensor (QDAS) based on an LFS Φ-OTDR, utilizing a discrete Rayleigh-enhanced single-mode fiber (eSMF). The mechanism of Doppler-induced crosstalk was analyzed, and the effects of pulse parameters, including pulse width, sweep rate, and bandwidth, were studied. Moreover, a discrete eSMF was proposed to suppress the crosstalk by reducing the change rate in the local phase. As a proof of concept, a vibration signal with a frequency of 8 kHz was successfully detected with a spatial resolution of 10 cm, a strain resolution of 190 pε/√Hz, and an improved crosstalk suppression of 20 dB. The proposed QDAS system with Doppler-induced crosstalk suppression is promising for ultrasonic structural health monitoring, such as aerial vehicles and deep-sea submersibles.

1. Introduction

Distributed acoustic sensor (DAS) has been widely used in intrusion detection [1], oil and gas industry [2], structural health monitoring [3] and geological detection [4] due to its capability of locating the vibration events on the fiber under test (FUT) and accurately reconstructing the acoustic wave. A key type of DAS is phase-sensitive optical time-domain reflectometry (Φ-OTDR), in which the demodulated phase change exhibits a linear relationship with the acoustic wave applied to the optical fiber [5–8]. In conventional Φ-OTDR systems, spatial resolution (SR) is determined by the width of the single-frequency probe pulse [9], leading to an inherent trade-off between SR and signal-to-noise ratio (SNR). To address this limitation, pulse-compression Φ-OTDR systems have been developed utilizing linear-frequency-swept (LFS) probe pulses combined with matched filter algorithm. It can decouple SR from pulse width [10]. For instance, Liu *et al.* developed a high-fidelity DAS system based on pulse compression and an intensity modulator, achieving an all-fiber intensity SNR of 30 dB and a SR of 0.8 m [11]. Moreover, we demonstrated a DAS system with a very high SR of 1.2 cm by utilizing a single-sideband modulator for positive and negative frequency sweeping [12].

The fundamental assumption in DAS system is the fiber remains stable during the probe pulse duration. However, in case the pulse passes through a vibration section, the vibration-induced phase modulation will vary over time, and hence leads to a Doppler shift in the Rayleigh backscattering (RBS) signal [13]. This phenomenon is similar to that encountered in conventional

#568572 https://doi.org/10.1364/OE.568572
Journal © 2025 Received 21 May 2025; revised 4 Sep 2025; accepted 17 Sep 2025; published 26 Sep 2025

Optics EXPRESS

radar [14]. The Doppler shift can induce distance offsets in the RBS signal in optical frequency domain reflectometry (OFDR) or LFS Φ-OTDR systems. This effect further leads to phase mismatches, resulting in crosstalk beyond the vibration area.

In recent years, several methods have been proposed to address this issue in OFDR system. For example, Zhu *et al.* proposed a time-frequency multiplexing method for reducing the phase modulation of probe light during each detection, thereby minimizing the crosstalk [15]. However, this approach limits the sweep frequency range, thus deteriorating SR. Moreover, the distance-correction-based compensation methods have also been reported. For example, Okamoto *et al.* proposed a Doppler-induced distance offset compensation by calculating the cross-correlation of RBS waveforms [16]. Liu *et al.* reported an adaptive 2D cross-correlation algorithm to correct beat frequency offsets, achieving a SR of 12 cm and a suppression of crosstalk up to 40.5 dB [17]. This method primarily relies on full-spectrum spectral-domain demodulation for offset compensation. For Φ-OFDR systems using phase demodulation, Xie *et al.* reported a frequency-tracking and spectrum-zooming algorithm, enabling high-fidelity strain reconstruction with a SR of 2.5 cm and a 30 dB improvement in SNR [18]. However, relevant analysis and compensation strategies for LFS Φ-OTDR remain lacking.

In this work, we report a Doppler-induced crosstalk suppression technique for LFS Φ-OTDR using a discrete eSMF. The Doppler shift in the RBS signal caused by vibration was characterized. The relationships between the crosstalk and detection pulses parameters, including pulse width, sweep rate and bandwidth, were studied. The crosstalk originates from the combination of the random phase distribution in the RBS signal and the Doppler-induced distance offset. To address this issue, a discrete eSMF was employed to reduce the local phase change rate, thereby effectively suppressing the crosstalk. As a proof of concept, a vibration signal with a frequency of 8 kHz was successfully recovered with a SR of 10 cm, a strain resolution of 190 pε/$\sqrt{\text{Hz}}$ and an improved crosstalk suppression of 20 dB. The proposed system could potentially be used in structural health monitoring field, such as aerial vehicles and deep-sea submersibles.

2. Principles and methods

2.1. Principle of LFS pules compression Φ-OTDR

The experimental setup of a pulse compression Φ-OTDR is shown in Fig. 1(a). Coherent light from the fiber laser (NKT X15) is split by a 1:9 polarization-maintaining fiber coupler. 10% of the light is used as the local oscillator (LO) and is input to an integrated coherent receiver (ICR, 22 GHz bandwidth, FUJITSU FIM24704). The remaining portion of light is modulated into a probe pulse by an I/Q modulator (20 GHz bandwidth, SUMITOMO), which is driven by an arbitrary waveform generator (AWG, Keysight M8195A) with a large LFS bandwidth. The probe pulse is then directed into an acousto-optic modulator (AOM, SGTF200-1550-1FH) to minimize pulse tailing and enhance the extinction ratio. The AOM driver is controlled by an arbitrary function generator (AFG, SDG6032X-E), which generates a square-wave pulse sequence with a specific time offset to synchronize with the pulses from the I/Q modulator. The probe pulse is amplified by an erbium-doped fiber amplifier (EDFA) and injected into the fiber under test (FUT) via a circulator. A piezoelectric transducer (PZT) is used to apply vibration. The RBS signal from the sensing fiber is fed into the signal port of the ICR. The beat signals between the LO and RBS signal are converted into photocurrent signals by balanced photodetectors in the ICR. These photocurrent signals are captured by an oscilloscope (OSC, Keysight DSOV254A). The AWG, AFG, and OSC are clock-synchronized, with both the AFG and OSC triggered by the AWG. Additionally, offline digital signal processing is performed on a personal computer.

The RBS signal arises from the refractive index inhomogeneity in fiber core, so the fiber can be modeled as a collection of uniformly distributed scattering centers. The position of the i^{th} scattering center is denoted by L_i, and its round-trip time is given by $\tau_i = 2nL_i/c$, where n is the effect refractive index of the fiber and c is the light velocity in vacuum. By mixing the RBS

Optics EXPRESS

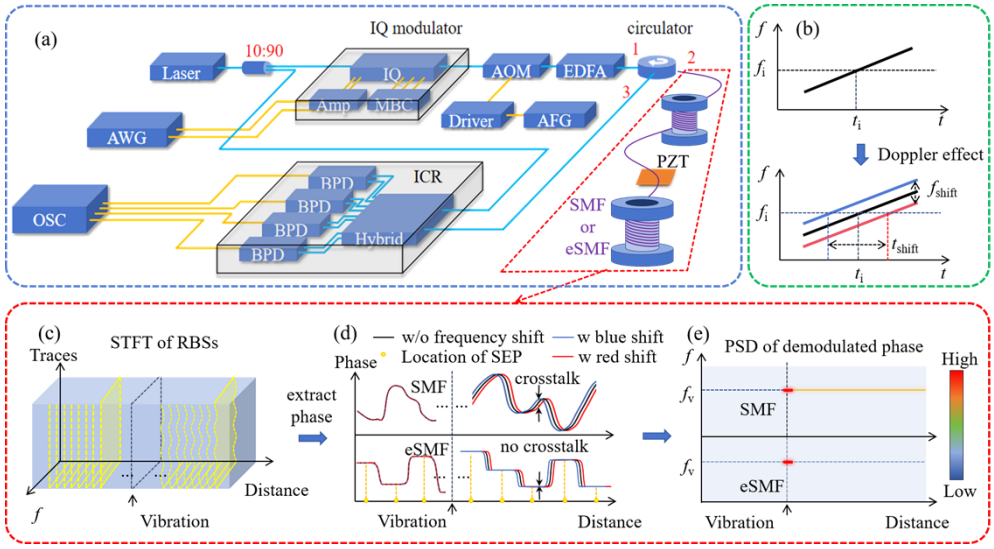

Fig. 1. (a) Experimental setup of the pulse compression Φ-OTDR. (b) Doppler shift induced by vibration in LFS pulse. (c) RBS spectra before and after the disturbed region of the sensing fiber. (d) The demodulated phase curves of SMF and eSMF. (e) The PSD of demodulated phase of SMF and eSMF.

signal with LO signal, the instantaneous photocurrent $i(t)$ of beat signal is given by

$$i(t) = \sum_{i=1}^{M} A_i W(\frac{t-\tau_i}{T_p}) \cdot \sin[2\pi f_0(t-\tau_i) + \pi\kappa(t-\tau_i)^2 - \omega_c\tau_i - \varphi_i(t)] \,, \tag{1}$$

where A_i is the amplitude of scattering light, $W(t)$ is the rectangular window, T_p is the pulse duration, M is the total number of scattering centers, ω_c is the center frequency of the laser, $\varphi_i(t)$ is the phase change induced by dynamic strain, f_0 and κ are the initial frequency and frequency sweep rate of modulation signal, respectively. The dynamic strain $\varepsilon(t)$ and the phase change $\varphi_i(t)$ are linearly related as [17]

$$\varphi_i(t) = \begin{cases} 0, & L_i < L_s \\ \frac{4\pi n}{\lambda} \cdot 0.78(L_i - L_s)\varepsilon(t), & L_s < L_i < L_e, \\ \frac{4\pi n}{\lambda} \cdot 0.78(L_e - L_s)\varepsilon(t), & L_e < L_i \end{cases} \tag{2}$$

where L_s and L_e represent the positions of the starting and the ending points of the vibrated fiber section, respectively. By applying a matched filter and I/Q demodulation algorithm to the RBS signal, the phase along the entire optical fiber could be obtained. Subsequently, vibration information can be recovered using spatial and temporal differential operations.

The SR of pulse-compression Φ-OTDR is primarily determined by the bandwidth of the probe pulse. After the digital matched filter algorithm [19], the LFS pulse can be compressed into a spike-like function. The SR is defined by the full width at half maximum (FWHM) of the main lobe of the compressed function:

$$\Delta Z = \frac{c}{2nB} K_w, \tag{3}$$

where B is the bandwidth of the frequency sweep and K_w is the SR deteriorating coefficient induced by the frequency domain window shape.

Optics EXPRESS

2.2. Crosstalk induced by Doppler shift

The instantaneous frequency of each backscattering signal can be derived from the phase information as

$$f_i(t) = f_0 + \kappa t - \frac{d\varphi_i(t)}{2\pi \cdot dt}, \tag{4}$$

where the last term is the Doppler shift $f_D(t) = -d\varphi_i(t)/(2\pi \cdot dt)$. Here, we assume that $\varphi_i(t)$ varies approximately linearly within the duration of probe pulse to simplify the analysis. Therefore, the Doppler shift $f_D(t)$ is approximately constant for single detection. The Doppler shift $f_D(t)$ would generate time shift $\Delta t = -f_D(t)/\kappa$, as shown in Fig. 1(b). After matched filtering, the time shift Δt leads to a distance offset in the RBS signal behind the vibration section, as shown in Fig. 1(c)

$$\Delta d(t) = \frac{c \cdot \Delta t}{2n} = -\frac{c}{2n} \cdot \frac{f_D(t)}{\kappa}. \tag{5}$$

It is clear that the distance offset is inversely proportional to the sweep rate. As shown in Fig. 1(d), for a positive frequency sweep pulse, the Doppler red shift causes an increase in distance, while the Doppler blue shift results in a decrease in distance, respectively, both in SMF and eSMF. In standard SMF, the phase of the RBS signal is randomly distributed along the distance due to the random distribution of scattering centers. Under temporal differentiation, the Doppler-induced distance offset leads to phase errors, resulting in crosstalk. In contrast, the phase remains stable around the scattering-enhanced points (SEPs), thus eliminating phase errors. The average phase change rate k_φ is introduced to statistically characterize the local phase behavior. The corresponding average phase error can therefore be expressed as

$$\Delta\varphi(t) = \Delta d(t) \cdot k_\varphi. \tag{6}$$

Moreover, the power spectral densities (PSDs) of the demodulated phase were compared for SMF and eSMF under sinusoidal excitation. As shown in Fig. 1(e), crosstalk appears in the SMF, whereas it is effectively suppressed in the eSMF. It should be noted that the crosstalk occurs at the same frequency as the applied sinusoidal vibration, since the frequencies of the distance offset and the strain rate are identical, as indicated by Eq. (5).

2.3. Method of crosstalk compensation

According to Eq. (1), the RBS signal at each position L_i is formed by the coherent super-position of backscattered components within a spatial range of $cT_p/2n$. After applying a matched filter, this range is compressed to a spatial window centered at L_i with a length of ΔZ. Figure 2(a) shows the RBS signals of SMF under different SRs. The spatial windows with an SR of a and b are denoted as d_{ai} and d_{bi}, respectively, and their corresponding electric field vectors of RBS signal are represented as E_{ai} and E_{bi}. Note that the SR a is smaller than SR b, i.e., the spatial window d_{ai} is longer than d_{bi}. The position of d_{a2} is located Δl away from d_{a1}, where Δl is shorter than SR. As the probe pulse propagates over a distance Δl, the electric field vectors undergo a variation denoted as $E_{\Delta l}$. The corresponding phase shifts for SR a and b are represented by $\Delta\varphi_{a,\Delta l}$ and $\Delta\varphi_{b,\Delta l}$, respectively. The amplitude of the scattering vector E_{ai} is larger owing to more scattering centers within the spatial window d_{ai}. Consequently, for a comparable perturbation $E_{\Delta l}$, the resulting phase shift $\Delta\varphi_{a,\Delta l}$ is relatively smaller. Therefore, a lower SR is associated with a reduced rate of phase variation. To further quantify this trend, we performed simulations of the phase change rate of RBS signal under different modulation bandwidths, which define the spatial resolution in an LFS Φ-OTDR system [19]. The rate of phase variation was obtained using a spatial differentiation method. The vibration-free RBS signal was demodulated using the IQ algorithm to derive the phase curves at all positions. Subsequently, the phase curve of each RBS was differentiated point by point, and the mean absolute value over all positions was calculated.

Optics EXPRESS

As shown in Fig. 3, the simulated results indicate k_φ is linearly related to the swept bandwidth B and hence inversely proportional to ΔZ for SMF. This relationship can be expressed as

$$k_\varphi = \alpha \cdot B + \beta, \tag{7}$$

where α and β are the slope and intercept, respectively. Combining Eqs. (5), (6) and (7), the average amplitude of phase error could be expressed:

$$\Delta\varphi(t) = \Delta d(t) \cdot k_\varphi = \frac{c}{2n} \cdot \frac{f_D(t) \cdot (\alpha B + \beta)}{\kappa} \approx \frac{c\alpha}{2n} \cdot f_D(t) \cdot T_p. \tag{8}$$

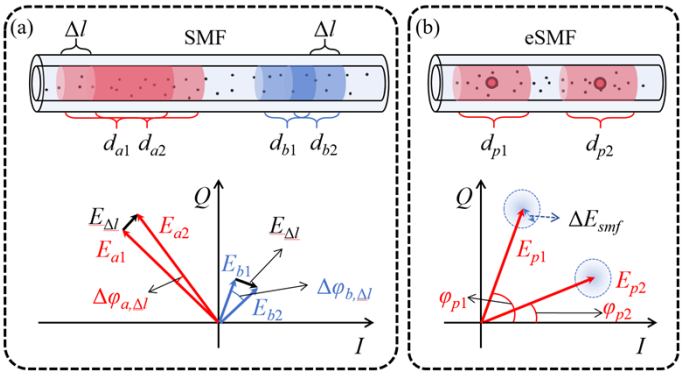

Fig. 2. (a) Scattering model and vector diagram of the RBS signal in SMF under different SRs. (b) Corresponding model and diagram in eSMF, highlighting reduced phase variation.

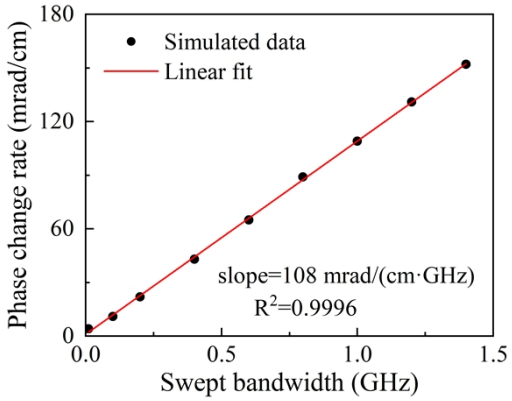

Fig. 3. Simulated phase change rate as a function of swept bandwidth in SMF.

Therefore, the phase error contributing to crosstalk is approximately proportional to the pulse width. Notably, the Doppler-induced distance offset and the random phase variations, characterized by the phase change rate, are the primary contributors to crosstalk.

In the case of small swept bandwidth within a certain pulse duration (i.e., low frequency sweep rates), the phase change rate is small, and excessive distance offset becomes the primary contributor to crosstalk. Correcting this distance offset in the RBS signal is effective for suppressing crosstalk. A common approach to estimate the distance offset is to calculate the cross-correlation between the spectra or phase traces. In the case of a large swept bandwidth (i.e.,

Optics EXPRESS

high sweep rates), the distance offset decreases while the phase change rate increases, keeping the average crosstalk amplitude nearly constant. Once the distance offset approaches the spatial sampling interval, correcting the distance in Φ-OTDR systems becomes challenging. In such cases, reducing the local phase change rate is an effective strategy.

Figure 2(b) illustrates the schematic of using eSMF to reduce the local phase change rate. Two highlighted points represent SEPs, which have significantly higher scattering coefficients than conventional Rayleigh scattering centers. The scattering signal from the i^{th} SEP is denoted as d_{pi}. The spatial window is chosen to be slightly shorter than the distance between adjacent SEPs to ensure high spatial resolution and large tolerance of distance offset. The corresponding electric field vector and phase are represented as E_{pi} and φ_{pi}, respectively. The vector superposition of RBS signal within the SR is denoted as ΔE_{smf}. Owing to the significant difference in scattering strength, the phase φ_{pi} of E_{pi} is minimally affected by ΔE_{smf}. Consequently, when the SR is shorter than the SEP spacing, the phase of the eSMF almost remains constant within each resolution window ΔZ, leading to a reduction in the local phase change rate. By demodulating the phase changes between two SEPs, the crosstalk is effectively suppressed.

3. Experimental results and discussions

3.1. Doppler-induced crosstalk in SMF

The Doppler-induced crosstalk in SMF was investigated. The FUT was a 30-meter-long SMF with a 20-cm section mounted on a PZT. A sinusoidal vibration with an amplitude of 1 V and frequency of 8 kHz was applied. The modulation frequency of the probe pulse was swept from 0.5 GHz to 4.5 GHz, with a repetition rate of 20 kHz and a pulse duration of 5 μs. In addition, the rotated-vector-sum algorithm and inner-pulse frequency-division was used for eliminating the signal fading [20]. The inner-pulse bandwidth was 2.5 GHz and the frequency interval was 0.75 GHz. In order to suppress the sidelobes, the rectangular window in Eq. (1) was replaced with a Hanning window at the cost of larger SR [21]. After pulse compression, the theoretical SR was approximately 8 cm. The gauge length used was set to 10 cm.

The vibration along the entire FUT was recovered using the proposed method. Figures 4(a) and 4(b) demonstrate the demodulated phase map and the vibration waveform near the PZT. Interference fading was eliminated effectively. The yellow curve represents a fitted sinusoidal waveform of measured data. The vibration frequency, determined from the PSD in Fig. 4(c), is 8 kHz with an SNR of 30 dB. The standard deviation distribution of demodulated phase is plotted in Fig. 4(d). The rising edge (10% to 90%) of the vibration signal spans 10.1 cm, indicating the system SR.

The frequency response along fiber is shown in Fig. 5(a), clearly revealing the presence of crosstalk beyond the PZT section. As shown in the inset of Fig. 5(b), the demodulated crosstalk at 20 m resembles white noise. However, its PSD exhibits a peak frequency at 8 kHz, corresponding to the applied vibration frequency. This confirms that the crosstalk frequency matches the excitation frequency, as both the sinusoidal signal and its rate of change share the same frequency. As shown in Fig. 5(c), the PSD at vibration frequency of fiber beyond PZT increases and the crosstalk is only 20 dB, which is weaker than vibration signal. Furthermore, the relationship between the crosstalk and pulse width was analyzed. The average crosstalk was calculated from the PSD at the vibration frequency f_v in the fiber section beyond the PZT. As shown in Fig. 5(d), the crosstalk increases linearly with the pulse width, which agrees well with the expectation from Eq. (8).

3.2. Characterization of Doppler shift

The Doppler shift was further studied using the experimental setup in Fig. 6(a). The probe light path and LO path are the same as in Fig. 1(a). To extract the Doppler shift, a reference fiber

Optics EXPRESS

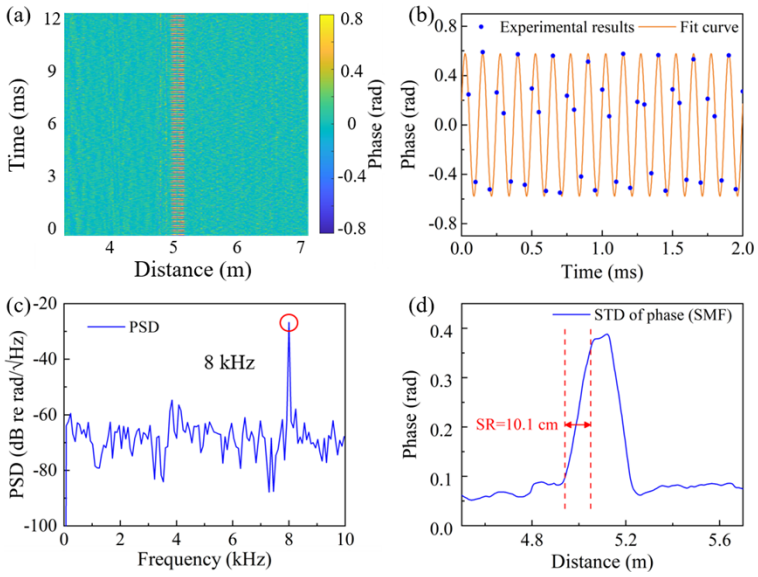

Fig. 4. Distributed vibration sensing results using SMF. (a) Demodulated phase map. (b) Reconstructed vibration waveform. (c) PSD of the vibration signal. (d) Standard deviation of the demodulated phase.

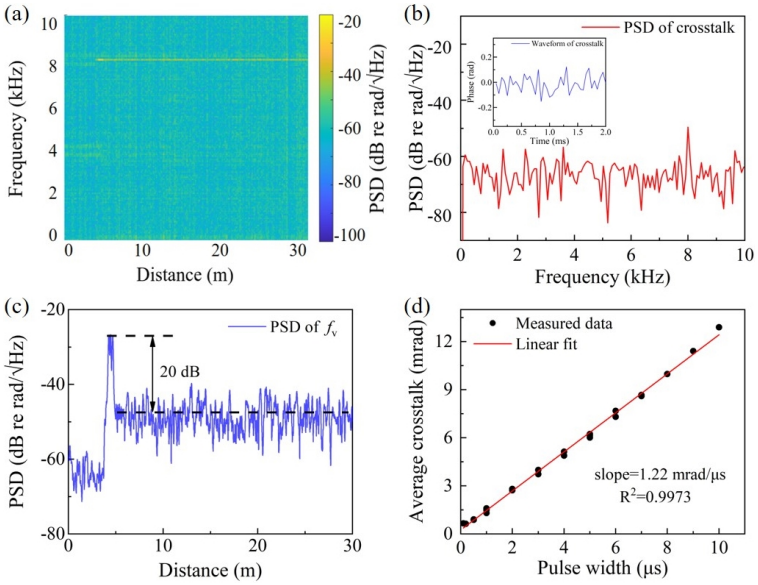

Fig. 5. Analysis of Doppler-induced crosstalk using SMF. (a) Frequency spectra along the fiber. (b) PSD and time-domain waveform of the crosstalk beyond the PZT. (c) Spatial distribution of vibration frequency along the fiber. (d) Average crosstalk as a function of pulse width.

Optics EXPRESS

without vibration was added. The lengths of two fibers are identical, and a disturbance is applied to one of them using a PZT actuator. For convenience, a fiber mirror (FM) is installed at each fiber end to replace the RBS signal with reflected light. The FM can be regarded as a scattering center with high reflectivity. The reflected probe pulses interfere with the LO signal, and the resulting beat signals were captured by a balanced photodetector (BDP, PDB480C) and recorded with an oscilloscope (OSC).

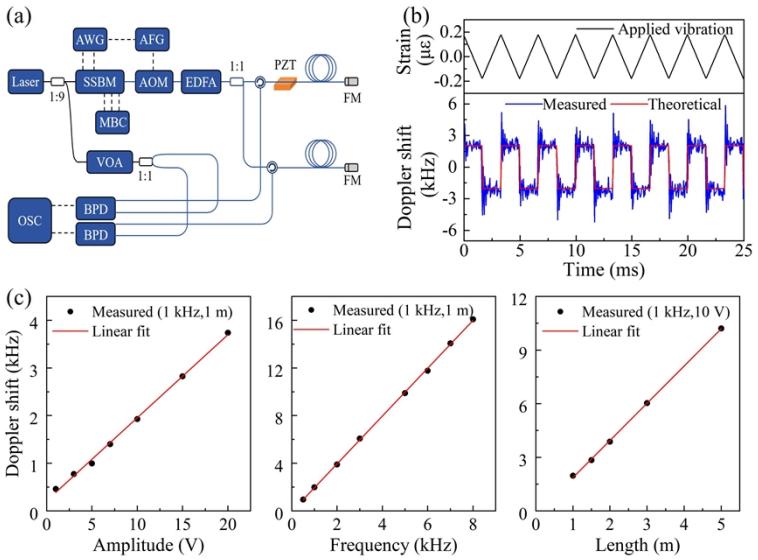

Fig. 6. Characterization of Doppler shift. (a) Experimental setup. (b) Time-domain waveforms of applied vibration and the corresponding Doppler shift. (c) The relationships between the Doppler shift and vibration parameters.

To obtain the Doppler shift, the phases in two beat signals were extracted and separately time-integrated. The difference in integral phase was then calculated and linearly fitted. The slope is $2\pi f_D(t) + 2\pi f_L$, where f_L is a negligible frequency offset caused by slight differences in fiber length. The applied vibration and measured Doppler shift are shown in Fig. 6(b). The vibration is a sawtooth wave, and the measured Doppler shift is a square wave, which consists with the theoretical expectations, i.e., the Doppler shift is in proportion to the strain rate. Moreover, the relationships between Doppler shift and vibration parameters were investigated. The Doppler shift was measured with increasing vibration and fixed vibration length and frequency. Then, we repeated the experiment with vibration frequency and length as variables, respectively. As shown in Fig. 6(c), the amplitude of Doppler shift is in proportion to the vibration amplitude, frequency and length, respectively. Note that the Doppler shift within a pulse width is not absolutely constant due to slight nonlinearity of vibration. Considering that the pulse width is in a microsecond range and the vibration frequency is in a kilohertz range, the vibration within the pulse width can be approximated as linear.

3.3. *Suppression of Doppler-induced crosstalk*

Suppression of the Doppler-induced crosstalk was achieved for both low and high frequency sweep rates. At first, a probe bandwidth of 200 MHz and a pulse width of 10 μs were used. A 180-meters-long SMF was used as the FUT. A sinusoidal vibration at 8 kHz was applied with a PZT at the position of ~ 60 m. As shown in Fig. 7(a), the spatial differential phase curves beyond the vibration region exhibit slow variation, and the Doppler-induced distance shift between successive interrogation traces could be seen. Figure 7(b) demonstrates this distance offset is

Optics EXPRESS

inversely proportional to the sweep rate, which agrees well with Eq. (5). The PSD along the FUT without compensation, as shown in Fig. 7(c), reveals significant crosstalk at the vibration frequency. A distance compensation method was implemented to mitigate this issue. The offset was estimated by computing the cross-correlation between adjacent phase traces and corrected in the distance domain. As shown in Fig. 7(d), this approach effectively suppresses the crosstalk along the entire fiber.

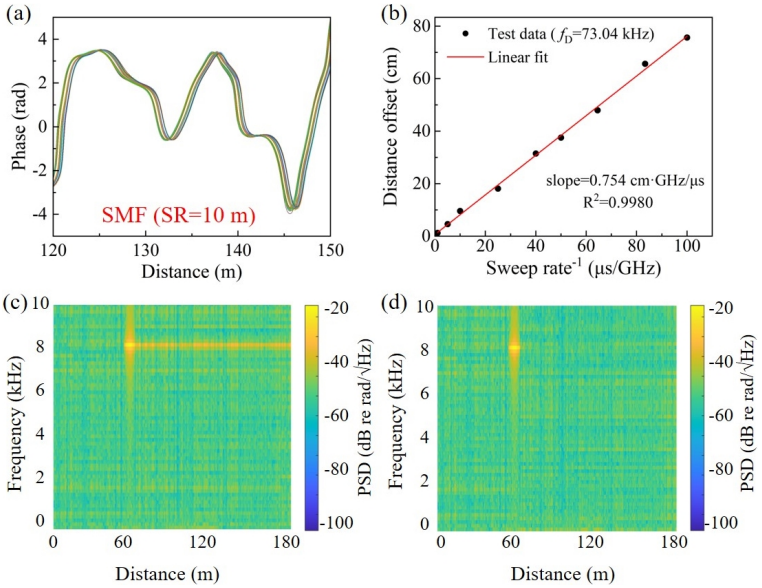

Fig. 7. (a) Spatial differential phase curves of an SMF under the conditions of low sweep rate and narrow modulation bandwidth. (b) Distance offset as a function of sweep rate. (c) PSD of SMF without compensation under low sweep rate conditions. (d) PSD after applying compensation under the same low sweep rate conditions.

Subsequently, the probe bandwidth of 4 GHz and a pulse width of 5 μs were used to study the crosstalk suppression under high sweep rate and large modulation bandwidth conditions. The FWHM in the main lobe of the compressed pulse is approximately 8 cm. The FUT was either a 30-meters-long SMF or an eSMF. The applied vibration parameters were identical to those in Section 3.1. The eSMF contains a series of longitudinal SEPs inscribed by using a femtosecond laser point-by-point method. The scattering rate of the SEPs is approximately -55 dB, with around 300 SEPs spaced at 10 cm intervals. The setup for automatic fabrication of the SEP array was detailed in our previous work [22,23]. The intensity and phase profiles of RBS signals in SMF and eSMF were extracted and shown in Fig. 8(a) and Fig. 8(b), with the SEPs highlighted in blue. In contrast to Fig. 7(a), the phase in SMF with larger bandwidth and higher sweep rate has more drastic variations, whereas the phase curve in eSMF is flatter near SEPs. Both SMF and eSMF RBS signals have small distance offsets due to the high sweep rate. Then, the local phase change rates of SMF and eSMF were calculated by spatial differentiation. As shown in Fig. 8(c), the phase change rate distribution is relatively random for SMF, but is smooth and close to zero near the SEPs for eSMF. Then, the average absolute phase change rates for different modulation bandwidths were calculated. For the SMF, the average was taken over all points, whereas for eSMF, only points around the SEPs were considered. As shown in Fig. 8(d), the average phase change rate in SMF increases linearly with the swept bandwidth. In contrast, for eSMF, the phase change rate remains consistently low, showing weak dependence on the modulation bandwidth.

Optics EXPRESS

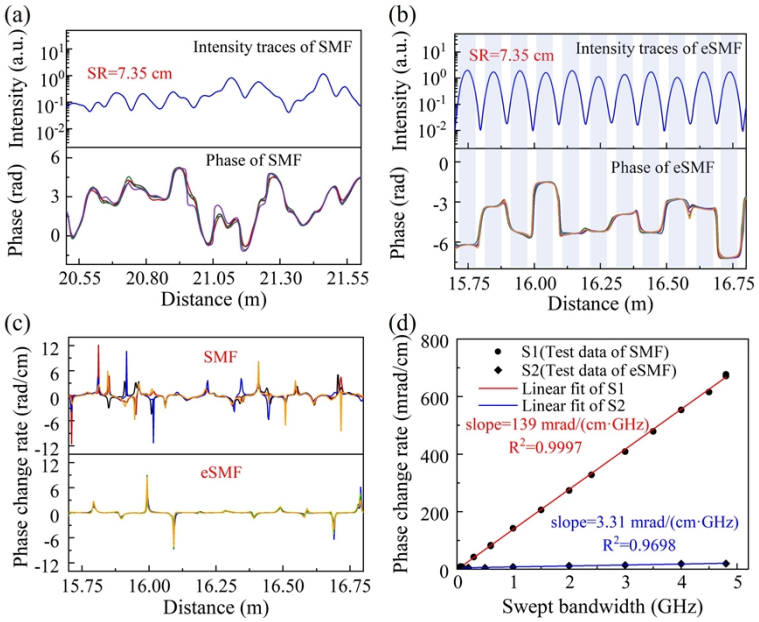

Fig. 8. Characteristics of RBS signal curves in SMF and eSMF under high sweep rate and large modulation bandwidth conditions. Intensity and phase distribution of RBS signals in (a) SMF and (b) eSMF. (c) Phase change rate distributions in SMF and eSMF. (d) Average phase change rates in SMF and eSMF under different swept bandwidths.

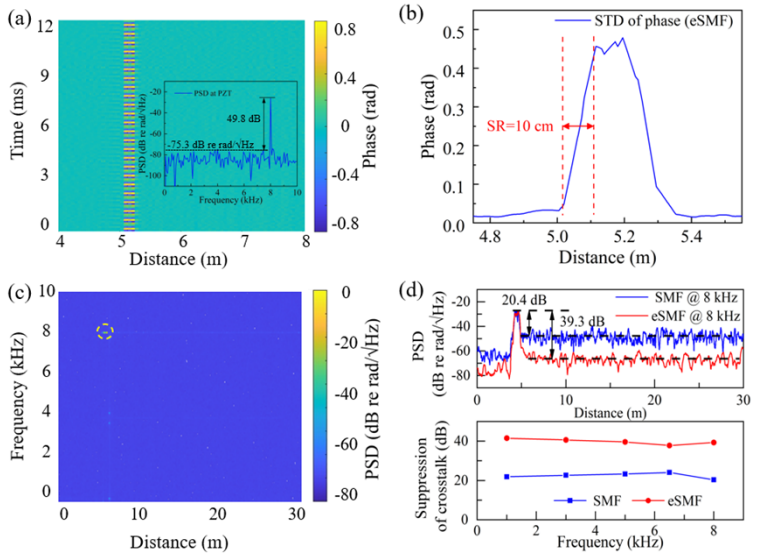

Fig. 9. Distributed vibration sensing using eSMF. (a) Demodulated phase map with an inset showing the PSD of demodulated vibration. (b) Standard deviation of the demodulated phase along the fiber. (c) Frequency spectra along the fiber. (d) Suppression of crosstalk in SMF and eSMF.

Therefore, after temporal differentiation, the phase error caused by distance offset in eSMF is significantly smaller than that in SMF.

Optics EXPRESS

Hence, the eSMF was used for Doppler-crosstalk suppression. As shown in Fig. 9(a), the applied vibration was recovered successfully. The inset shows the PSD of the demodulated phase, featuring a prominent peak at 8 kHz, an SNR of 49.8 dB, and a self-noise level of -75.3 dB re rad/$\sqrt{\text{Hz}}$, which corresponds to a strain sensitivity of 190 p$\varepsilon/\sqrt{\text{Hz}}$ [3]. Compared with the SMF, the noise floor is lower due to higher scattering intensity. The standard deviation of the phase along the fiber was calculated from 512 RBS traces. As shown in Fig. 9(b), the SR of QDAS is ~10 cm, recording from the trace rising edge. The frequency spectra along the fiber clearly reveal the vibration location, as illustrated in Fig. 9(c). Slight residual crosstalk remains at the vibration frequency due to the non-zero phase change rate near the SEP. A weak signal at 4 kHz is also observed, originating from the second harmonic of the Doppler shift induced by vibration nonlinearity. As shown in Fig. 9(d), the crosstalk suppression ratio with eSMF is enhanced by approximately 20 dB relative to the SMF. Furthermore, when the experiment was conducted at vibration frequencies ranging from 1 kHz to 8 kHz, the crosstalk suppression ratio with SMF was approximately 20 dB, whereas that with eSMF reached about 40 dB.

4. Conclusion

We have analyzed and suppressed the Doppler-induced crosstalk in LFS pulse compression Φ-OTDR system. Dynamic strain introduces a Doppler shift, resulting in the crosstalk due to the random phase distribution of the RBS signal and the Doppler-induced distance offset. The mechanism of Doppler-induced crosstalk was analyzed, and the effects of pulse parameters, including pulse width, sweep rate, and bandwidth, were thoroughly investigated. In the case of low SR, the crosstalk could be compensated by correcting the distance offset, while in the case of high SR, the crosstalk could be further suppressed by reducing the local phase change rate by using scattering enhanced fiber, i.e., eSMF. As a proof of concept, a vibration with a frequency of 8 kHz is successfully recovered with a SR of 10 cm and a strain resolution of 190 p$\varepsilon/\sqrt{\text{Hz}}$. The suppression ratio of crosstalk is improved by 20 dB compared with SMF. Consequently, the proposed method could potentially be used in structural health monitoring field, such as aerial vehicles and deep-sea submersibles.

Funding. National Natural Science Foundation of China (62222510, 62435012); LingChuang Research Project of China National Nuclear Corporation (CNNC-LCKY-202259); China Postdoctoral Science Foundation (2024M762125).

Disclosures. The authors declare no conflicts of interest.

Data availability. Data underlying the results presented in this paper are not publicly available at this time but may be obtained from the authors upon reasonable request.

References

1. Z. Li, J. Zhang, M. Wang, *et al.*, "Fiber distributed acoustic sensing using convolutional long short-term memory network: a field test on high-speed railway intrusion detection," Opt. Express **28**(3), 2925–2938 (2020).
2. I. Ashry, Y. Mao, B. Wang, *et al.*, "A review of distributed fiber–optic sensing in the oil and gas industry," J. Lightwave Technol. **40**(5), 1407–1431 (2022).
3. P. G. Hubbard, J. Xu, S. Zhang, *et al.*, "Dynamic structural health monitoring of a model wind turbine tower using distributed acoustic sensing (DAS)," J. Civil. Struct. Health Monit. **11**(3), 833–849 (2021).
4. T. Okamoto, D. Iida, and Y. Koshikiya, "Distributed acoustic sensing of seismic wave using optical frequency domain reflectometry," J. Lightwave Technol. **41**(22), 7036–7044 (2023).
5. H. Qian, B. Luo, H. He, *et al.*, "Phase demodulation based on DCM algorithm in Φ-OTDR with self-interference balance detection," IEEE Photonics Technol. Lett. **32**(8), 473–476 (2020).
6. Y. Wakisaka, H. Takahashi, D. Iida, *et al.*, "Broad-bandwidth and accurate optical vibration sensing by using FDM Φ-OTDR with linear regression analysis of multi-frequency phase responses," Opt. Express **31**(17), 27990–28009 (2023).
7. X. He, S. Xie, F. Liu, *et al.*, "Multi-event waveform-retrieved distributed optical fiber acoustic sensor using dual-pulse heterodyne phase-sensitive OTDR," Opt. Lett. **42**(3), 442–445 (2017).
8. M. Nie, J. Xu, J. Yu, *et al.*, "Ultra long single span distributed sensing distance over 200 km based on the phase-sensitive OTDR with bidirectional high-order raman amplification," in *Proc. 19th Int. Conf. Opt. Commun. Netw*, 01–03 (2021).

Optics EXPRESS

9. Z. Wang, B. Lu, Q. Ye, *et al.*, "Recent progress in distributed fiber acoustic sensing with Φ-OTDR," Sensors **20**(22), 6594 (2020).
10. W. Zou, S. Yang, X. Long, *et al.*, "Optical pulse compression reflectometry: proposal and proof-of-concept experiment," Opt. Express **23**(1), 512–522 (2015).
11. D. Chen, Q. Liu, and Z. He, "High-fidelity distributed fiber-optic acoustic sensor with fading noise suppressed and sub-meter spatial resolution," Opt. Express **26**(13), 16138–16146 (2018).
12. X. Xiao, J. He, B. Du, *et al.*, "High-spatial-resolution distributed acoustic sensor utilizing a positive- and negative-swept pulse," J. Lightwave Technol. **42**(8), 2991–2996 (2024).
13. H. Li, Q. Liu, D. Chen, *et al.*, "High-spatial-resolution fiber-optic distributed acoustic sensor based on Φ-OFDR with enhanced crosstalk suppression," Opt. Lett. **45**(2), 563–566 (2020).
14. E. Raei, M. Modarres-Hashemi, and M. R. Bhavani Shankar, "Range cell migration correction by fractional fFourier transform in synthetic aperture radars," in *20th International Radar Symposium (IRS)* 1–10 (2019).
15. Z. Zhong, T. Liu, H. Wu, *et al.*, "High-spatial-resolution distributed acoustic sensor based on the time-frequency-multiplexing OFDR," Opt. Lett. **48**(21), 5803–5806 (2023).
16. T. Okamoto, D. Iida, and H. Oshida, "Vibration-induced beat frequency offset compensation in distributed acoustic sensing based on optical frequency domain reflectometry," J. Lightwave Technol. **37**(18), 4896–4901 (2019).
17. H. Li, Q. Liu, Y. Chang, *et al.*, "Analysis and compensation of vibration induced beat frequency shift in OFDR based fiber-optic distributed acoustic sensor," J. Lightwave Technol. **41**(1), 381–392 (2023).
18. Q. Yang, W. Xie, C. Wang, *et al.*, "Dynamic strain sensing using Doppler-shift-immune phase-sensitive OFDR with ultra-weak reflection array and frequency-tracking," Opt. Express **32**(25), 44816–44828 (2024).
19. Q. Liu, X. Fan, and Z. He, "Time-gated digital optical frequency domain reflectometry with 1.6-m spatial resolution over entire 110-km range," Opt. Express **23**(20), 25988–25995 (2015).
20. D. Chen, Q. Liu, and Z. He, "Phase-detection distributed fiber-optic vibration sensor without fading-noise based on time-gated digital OFDR," Opt. Express **25**(7), 8315–8325 (2017).
21. D. Chen, Q. Liu, X. Fan, *et al.*, "Distributed fiber-optic acoustic sensor with enhanced response bandwidth and high signal-to-noise ratio," J. Lightwave Technol. **35**(10), 2037–2043 (2017).
22. X. Xiao, B. Xu, X. Xu, *et al.*, "Femtosecond laser auto-positioning direct writing of a multicore fiber Bragg grating array for shape sensing," Opt. Lett. **47**(4), 758–761 (2022).
23. B. Xu, G. Chen, Z. Peng, *et al.*, "Distributed acoustic sensing in harsh environments based on femtosecond laser-inscribed ultra-short fiber Bragg grating arrays," Opt. Lett. **50**(10), 3337–3340 (2025).

https://doi.org/10.1364/OE.574135